# Dual-Band Wireless Power Transfer with Reactance Steering Network and Reconfigurable Receivers

Ming Liu, *Member, IEEE,* Minjie Chen, *Member, IEEE*

***Abstract*—Wireless power transfer (WPT) via near-field magnetic coupling is an enabling technology for many applications. A few WPT standards are under development with frequencies ranging from kHz to MHz. kHz operation offers higher power rating and MHz operation offers smaller size. This paper presents a dual-band WPT architecture with novel transmitter and receiver topologies that can achieve high performance at both 100 kHz and 13.56 MHz with low component count and decoupled power delivery at different frequencies. On the transmitter side, we introduce an enhanced push-pull Class-E topology together with a reactance steering network (RSN) which can seamlessly compensate the load impedance variation for MHz wireless power transmitters. On the receiver side, we present a reconfigurable dual-band rectifier that can achieve a power density of 300 W/inch$^3$ with low component count and low total harmonic distortion (THD). A complete dual-band WPT system comprising a RSN-based dual-band transmitter and multiple reconfigurable receivers has been built and tested. The WPT system can simultaneously deliver a total of 30 W of power to multiple receivers (15 W maximum each) with 82.5% efficiency at 100 kHz and 74.8% efficiency at 13.56 MHz with 2.8 cm of coil distance and up to 5 cm of coil misalignment.**

***Index Terms*—Dual-band wireless power transfer, reactance steering network, reconfigurable rectifier, high frequency power conversion, radio-frequency power amplifiers.**

## I. Introduction

Wireless power transfer (WPT) through near-field magnetic coupling is an enabling technology for many applications including consumer electronics and industrial applications [1]–[5]. A few WPT standards have been established (e.g., AirFuel, Qi) with frequencies ranging from hundreds of kHz to a few MHz. These standards may merge and may cover many frequency domains in the future. In general, there is a fundamental tradeoff between kHz operation and MHz operation in WPT: MHz operation enables long distance power transfer and better robustness against coil misalignment, while kHz operation offers higher efficiency and higher power transfer capability [6]. Both kHz and MHz WPT systems may co-exist for a long period of time. Many WPT equipped devices may co-locate in the same electromagnetic domain in many application scenarios (e.g., wireless powered desktop, wireless powered working bench). Emerging designs also need to be back-compatible with previous standards and need to be software upgradable (e.g., WPT in vehicles and robotics). High performance multi-band transmitters that can power multiple receivers at different frequencies, and miniaturized multi-band receivers that can receive power from a variety of transmitters are needed and are the main focus of this paper.

M. Liu and M. Chen (Corresponding author) are with the Department of Electrical Engineering and with the Andlinger Center for Energy and the Environment, Princeton University, Princeton, NJ 08540, USA (Email: ml45@princeton.edu, minjie@princeton.edu).

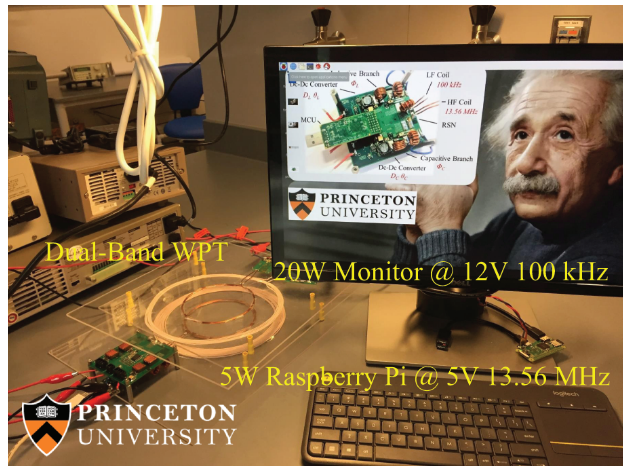


Fig. 1. A dual-band "complete" wireless desktop computer developed at Princeton Powerlab. The system simultaneously powers a 5 W Raspberry Pi at 13.56 MHz and a 20 W monitor at 100 kHz. The system is wirelessly powered and wirelessly connected to the internet.

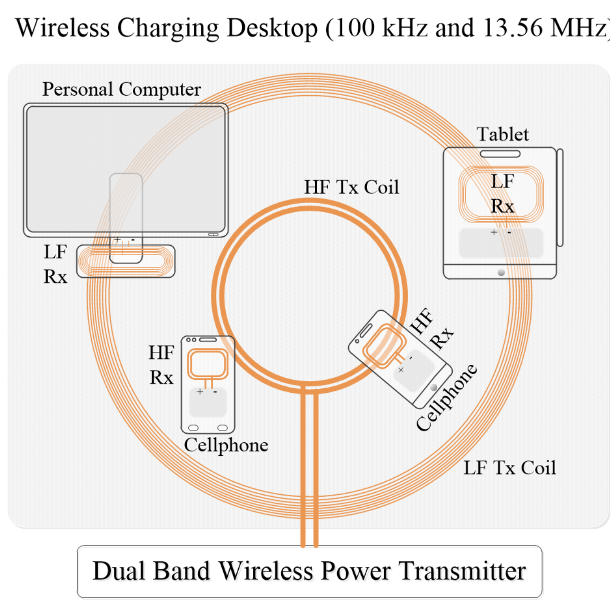


Fig. 2. Coil placement of a dual-band WPT desktop with multiple receivers operating at high frequency (HF, 13.56 MHz) and low frequency (LF, 100 kHz). The multiple receiving devices can be freely moved around and be continuously charged.

Many dual-band WPT systems have been developed [7]–[12]. Full-bridge inverter topologies are highly preferable in the kHz range, and single switch Class-E derived topologies are widely used in the MHz range. These existing solutions usually focus on the design of the passive network and the coils. This paper aims to push the performance boundary of dual-band WPT with better transmitter and receiver architectures. In the MHz range, maintaining resistive load is critical (e.g., for Class-E converters [13]). There exist many design techniques that can compress the load resistance variation [14]–[21]. However, for reactance variation, the most commonly-adopted solution is to use a separate tunable matching network (TMN) [22]. [23] presents a variable reactance rectifier which helps to address the challenge from the receiver side. However, the additional passive components and switching devices increase the component count and the volume. On the receiver side, full-bridge rectifiers can offer high efficiency and high tolerance to impedance variation for 100 kHz operation. For MHz operation, Class-E based rectifiers are very promising as they offer high performance with low component count and low total harmonic distortion (THD). Since receivers are usually co-packaged with portable devices or electric vehicles with size and thermal limits, low component count and small size are attractive [24].

This paper presents a few novel WPT topologies and architectures on both the transmitter side and the receiver side to achieve high efficiency with wide impedance variation range and low component count. Advantages are created by adopting the Multitrack and partial power processing concepts [25]–[28]. On the transmitter side, we introduce a reactance steering network (RSN) enabled dual-band transmitter [29] which can independently modulate the power delivered at two frequencies. On the receiver side, we present a reconfigurable dual-band receiver that can maintain high performance at both frequencies with low switch count and high power density. The dual-band receiver functions as a synchronous half-bridge rectifier at 100 kHz, and functions as two series-stacked Class-E rectifiers at 13.56 MHz. Many components are reused at both frequencies. An on-line impedance estimation method was proposed to maintain ZVS of the HF inverters. The prototype RSN transmitter can simultaneously deliver 30 W of power to multiple dual-band receivers (15 W maximum each) with 74.8% peak efficiency at 13.56 MHz with significant coil misalignment, and 82.5% peak efficiency at 100 kHz.

Fig. 1 shows a demo wireless desktop where a dual-band transmitter simultaneously powers a 5 W Raspberry Pi at 13.56 MHz and a 20 W monitor at 100 kHz. The Raspberry Pi interfaces with the monitor through HDMI. Other IoT devices that support wireless charging may be added. The full demo desktop is completely wireless: it is wirelessly powered and wirelessly connected to the internet. Fig. 2 shows the coil placement diagram. The transmitting coils and the receiving coils may be loosely coupled or closely coupled. The load impedance on the transmitter side may change across a wide range. The transmitter needs to maintain high performance at both kHz and MHz, and the receivers need to receive power from multiple frequencies with low component count.

The remainder of this paper is organized as follows: Section II provides an overview of the reconfigurable dual-band WPT system. The circuit topology and operation principles of the reactance steering network (RSN) and the RSN-based

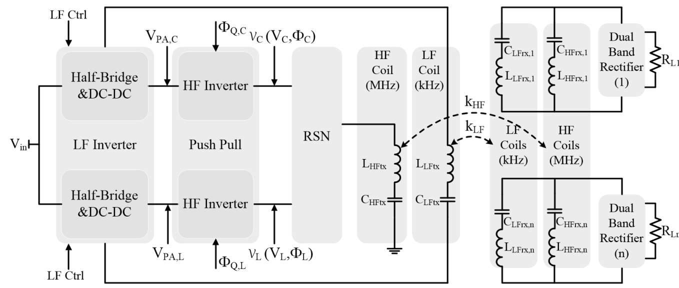


Fig. 3. Block diagram of a dual-band WPT system comprising a RSN-based dual-band transmitter and multiple reconfigurable dual-band receivers with different coupling coefficients.

dual-band transmitter are presented in Section III. Section IV introduces the topology and operation principles of the reconfigurable dual-band receiver. Section V presents the prototype and experimental results, including detailed theoretical analysis and measured results of the dual-band transmitter and receiver. Finally, Section VI concludes this paper.

## II. Overview of Dual-Band Multi-Receiver WPT

Fig. 3 shows the block diagram of the proposed dual-band WPT system including a RSN-based transmitter and multiple reconfigurable dual-band receivers. The RSN-based transmitter comprises two low frequency (LF) dc-dc converters operating at kHz (e.g., 100 kHz), one modified push-pull high frequency (HF) Class-E inverter operating at MHz (e.g., 13.56 MHz), a RSN, a LF transmitting coil, and a HF transmitting coil. The receiver side comprises multiple LF/HF receiving coils and multiple dual-band rectifiers. The two dc-dc converters modulate the two inputs of the modified push-pull Class-E inverter, and simultaneously drive the LF transmitting coil at 100 kHz. By modulating the voltage amplitude and the phase of the two HF inverters [29], the two inverter branches see pure resistive load. The dc-dc converters also drive the LF transmitting coil as a phase-shift full bridge inverter, transferring power at LF to the receivers.

Each of the function block in the RSN-based transmitter can be implemented in multiple ways: the LF inverters can be implemented as Class-D or full-bridge inverters; the low-pass filters at the output of the LF inverters can be implemented as L-networks or $\pi$-networks; the push-pull inverters can be implemented as Class-E, Class-F or Class-$\Phi$ inverters; the RSN can be implemented as a three-port LC network or other three-port network options. The LF and HF transmitting and receiving coils are standard coils tuned for nominal coupling. The two half-bridge circuits drive the LF coil, and the two HF inverters drive the HF coil. The power delivered at the two frequencies can be modulated independently.

The receiver developed in this paper is a dual-band reconfigurable receiver that can operate at either 100 kHz or 13.56 MHz. The receiver functions as two series-stacked Class-E rectifier at 13.56 MHz, and functions as a half-bridge rectifier at 100 kHz. It has very low component count and can maintain high performance at both frequencies. A single dual-band receiver can be reprogrammed to function at either frequency, and multiple receivers working at different

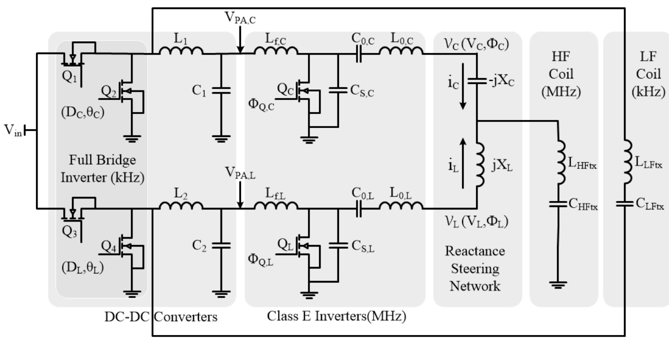


Fig. 4. Schematic of an example dual-band transmitter comprising a RSN, two HF Class-E inverters, two buck converters (with one half-bridge and one inductor) and two optimally tuned transmitting coils (one for each frequency).

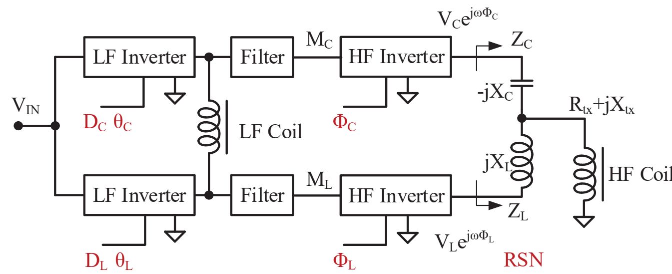


Fig. 5. Simplified block diagram of the RSN architecture. This architecture has six input variables: $D_C$, $D_L$, $\theta_C$, $\theta_L$, $\Phi_C$, $\Phi_L$, and independently drives two coils at two frequencies.

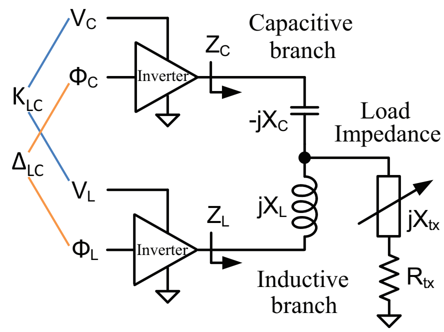


Fig. 6. Operation principles of the RSN. Amplitude and phase modulation of the high frequency inverters steer power between the two branches and perform reactance compensation. $V_C$, $V_L$, $\Phi_C$, $\Phi_L$ are the control variables.

frequencies can be placed in adjacent to each other while all maintaining high performance. The transmitter sees the impedance of all receivers operating at two frequencies with their power added together. Finally, the RSN-based transmitter and the dual-band reconfigurable receiver are merged together as a complete dual-band WPT system that operate at both frequencies. The transmitter can dynamically estimate the lumped load impedance and individually modulate the power delivered at each frequency.

## III. Dual-Band RSN Transmitter with a Modified Push-Pull Class-E Inverter

Fig. 4 shows the schematic of an example implementation of the RSN-based dual-band transmitter. It comprises two half-bridge low frequency inverters, two LC low pass filters, and two high frequency Class-E inverters. The two half-bridge inverters and the two low-pass filters function as two buck converters that modulate the inputs of the two Class-E inverters. The two Class-E inverters are loaded with a LC resonant network including an inductive branch $jX_L$ and a capacitive branch $-jX_C$. The two Class-E inverters and the LC resonant network can be interpreted as a modified push-pull Class-E inverter. The two half-bridge inverters also drive a low frequency coil as a full bridge inverter.

This RSN transmitter has the same component count as a traditional full-bridge inverter for LF operation and a push-pull Class-E inverter for HF operation. The key innovation of this design is to merge the LF and HF operation and maintain ZVS operation of the HF inverters against coil misalignment.

### *A. Principles of the Reactance Steering Network (RSN)*

Fig. 5 shows a simplified block diagram of the dual-band transmitter with a RSN connected between the push-pull Class-E inverter and the HF coil. The reactance steering network is a three terminal network comprising an inductor and a capacitor. Derived from the RCN [14], [15], Outphasing [16], and the ICN [18]–[20] concept, with modulated inverter dc inputs, the RSN splits the power flow to compensate the load impedance variation, so that the HF inverters can operate efficiently across a wide impedance range.

The RSN architecture has six control variables: $D_C$ and $D_L$ are the duty ratios of the two LF inverters; $\theta_C$ and $\theta_L$ are the phases of the two dc-dc converters; $\Phi_C$ and $\Phi_L$ are the phases of the two HF inverters. The two intermediate dc voltages $M_C$ and $M_L$ are controlled by $D_C$ and $D_L$. To simplify the analysis, we assume $X_C = X_L = X_O$ and model the two HF inverters as two ac voltage sources: $V_C^* = V_C e^{j\Phi_C}$ and $V_L^* = V_L e^{j\Phi_L}$. $X_O$ is the reactance of the inductive/capacitive branch. $X_L$ and $X_C$ are assumed to be equal to $X_O$. The amplitudes ($V_L$, $V_C$) and phases ($\Phi_L$, $\Phi_C$) can be independently modulated. Applying superposition rules, the effective load impedance of the two inverters, $Z_C$ and $Z_L$, are explicit functions of $X_O$, $R_{tx}$, $X_{tx}$ and $K_{LC}^*$:

$$Z_C = \frac{X_O^2}{R_{tx} - K_{LC}^* R_{tx} + (X_{tx} + X_O - K_{LC}^* X_{tx})j}, \quad (1)$$

$$Z_L = \frac{X_O^2}{R_{tx} - \frac{1}{K_{LC}^*} R_{tx} + (X_{tx} - X_O - \frac{1}{K_{LC}^*} X_{tx})j}. \quad (2)$$

$K_{LC}^*$ is the complex voltage ratio between the inductive branch and capacitive branch: $K_{LC}^* = \frac{V_L}{V_C} e^{j(\Phi_L - \Phi_C)}$. To ensure pure resistive $Z_C$ and $Z_L$, we need:

$$K_{LC} = \frac{V_L}{V_C} = \frac{X_{tx}\cos(\Delta_{LC}) - R_{tx}\sin(\Delta_{LC})}{X_{tx} - X_O}, \quad (3)$$

$$\sin^2(\Phi_L - \Phi_C) = \sin^2 \Delta_{LC} = \frac{X_O^2}{X_{tx}^2 + R_{tx}^2}. \quad (4)$$

Here $\Delta_{LC} = \Phi_L - \Phi_C$ is the phase difference between the two HF inverters. For a load impedance range $R_{tx} \in [R_{min}, R_{max}]$, $X_{tx} \in [X_{min}, X_{max}]$, $X_O$ should be selected such that $X_O^2 \leq (X_{tx}^2 + R_{tx}^2)$ holds true across the entire $R_{tx}$ and $X_{tx}$ range, so that there is a solution for $\Delta_{LC}$. For each pair of $R_{tx}$ and $X_{tx}$, there are four feasible solutions for $K_{LC}^*$, one located in each quadrant. Due to phase and polarity symmetry, the solution in the $1^{st}$ quadrant is equivalent to the solution in the $3^{rd}$ quadrant; and the solution for the $2^{nd}$ quadrant is equivalent to the solution in the $4^{th}$ quadrant. Usually, the solution in the $1^{st}$ (or $3^{rd}$) quadrant is preferable because the range of $K_{LC}$ in the $1^{st}$ quadrant is smaller than the range of $K_{LC}$ in the $2^{nd}$ (or $4^{th}$) quadrant. For example, according to the Eq. (3) and Eq. (4), the range of $K_{LC}$ in the $1^{st}$ quadrant is from 0.707 to 1.414 and the range of $K_{LC}$ in the $2^{nd}$ is from 0.007 to 140.7, when $R_{tx}$ =1Ω, $X_O = 1j\Omega$, and $X_{tx}$ varies from $-0.99j\Omega$ to $0.99j\Omega$. Thus, a first quadrant solution of $K_{LC}^*$ is preferable because keeping $\Delta_{LC}$ close to zero can minimize the converter stress. The optimal solutions for $K_{LC}$ and $\Delta_{LC}$ are:

$$K_{LC} = |\frac{V_L}{V_C}| = |\frac{X_O + X_{tx}}{X_{tx}\cos(\Delta_{LC}) + R_{tx}\sin(\Delta_{LC})}|. \quad (5)$$

$$\Delta_{LC} = \Phi_L - \Phi_C = \arcsin\sqrt{\frac{X_O^2}{X_{tx}^2 + R_{tx}^2}}. \quad (6)$$

For a typical voltage source inverter, $V_L$ is linearly proportional to $M_L$ and $D_L$, and $V_C$ is linearly proportional to $M_C$ and $D_C$. As a result, pure-resistive loading of the two HF inverters can be achieved by modulating $D_C$, $D_L$, $\Phi_C$ and $\Phi_L$. The control strategy for these variables are:

- If $Z_{tx}$ is resistive, the two HF inverters equally share power and both see pure resistive load;
- If $Z_{tx}$ is inductive, the system steers power towards the capacitive branch. The capacitive element $-jX_C$ is used to compensate the inductive load $Z_{tx}$;
- If $Z_{tx}$ is capacitive, the system steers power towards the inductive branch. The inductive element $jX_L$ is used to compensate the capacitive load $Z_{tx}$;

Fig. 6 illustrates the principles of the reactance steering network. The amplitude and phase modulation of the two HF inverters (power amplifiers) steer power between the two branches of the RSN and dynamically compensate for the load reactance variation.

We quantitatively present the design of an example RSN system in detail: assume $R_{tx}$ varies from 1Ω to 5Ω; $X_{tx}$ varies from $-2j\Omega$ to $2j\Omega$; and $X_O$ is selected as $1j\Omega$. Based on KCL and KVL, the effective resistances seen at the inductive branch ($R_L$) and capacitive branch ($R_C$) can be calculated based on Eq. (1) and Eq. (2), respectively. $R_L$ and $R_C$ can be used to estimate the power sharing between the two branches. Fig. 7a–Fig. 7d show the $K_{LC}$, $\Delta_{LC}$, $R_L$ and $R_C$ as functions of $R_{ts}$ and $X_{ts}$. As derived in [29], a voltage amplitude ratio adjustable from $1/\sqrt{2}$ to $\sqrt{2}$, and a phase shift adjustable from 0° to 90° can cover an arbitrary load impedance range.

As shown in Fig. 7, with an inductive load ($X_{tx} > 0$), $V_L$ should be larger than $V_C$ to deliver more power through the capacitive branch; with a capacitive load ($X_{tx} < 0$), $V_L$ should be smaller than $V_C$ to deliver more power through the inductive branch. When $|X_{tx}| \leq |X_O|$, both $R_L$ and $R_C$ are higher than the overall load resistance, indicating that the two inverters are sharing power. When $|X_{tx}| > |X_O|$ (i.e., the load reactance is very high), one of $R_L$ and $R_C$ is smaller than the overall load resistance, and the other one is negative, indicating that there exists circulating power between the two branches. In other words, when needed, one inverter branch functions as a rectifier to compensate the reactance variation.

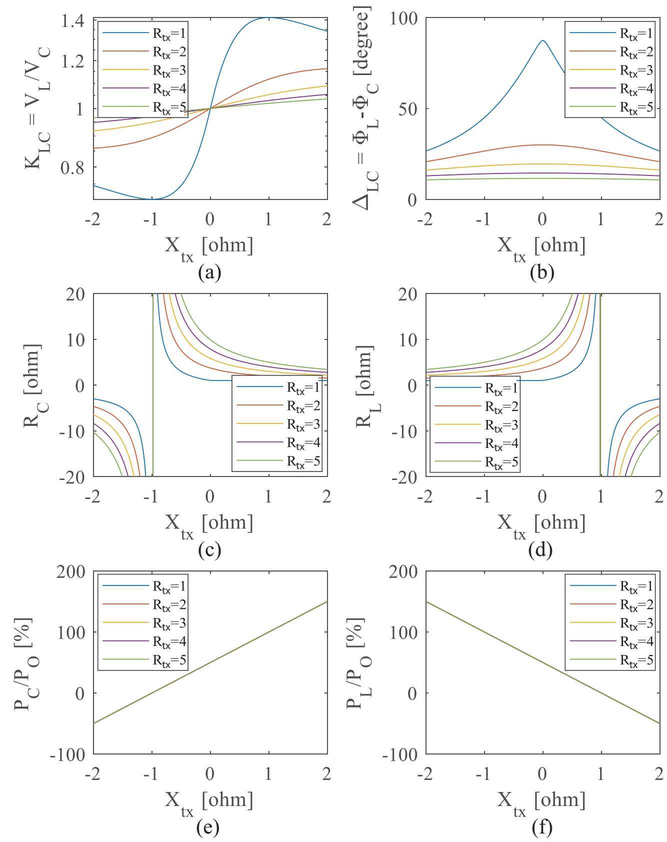


Fig. 7. Control variables as functions of the load reactance $X_{tx}$: (a) $V_L/V_C$; (b) $\Delta_{LC}$; (c) Resistance of the capacitive branch; (d) Resistance of the inductive branch; (e) Percentage of the power on the capacitive branch; (f) Percentage of the power on inductive branch. $P_C$: Power of the capacitive branch; $P_L$: Power of the inductive branch; $P_O$: Output power.

Fig. 7e and Fig. 7f show the percentage of the power sharing between the inductive and capacitive branches for this example RSN design. As expected, with pure resistive loads (i.e., $X_{tx} = 0$), the two branches evenly share power (50% each branch); with capacitive loads ($X_{tx} < 0$), the inductive branch delivers more power than the capacitive branch; with inductive loads ($X_{tx} > 0$), the capacitive branch delivers more power than the inductive branch; with very high capacitive loads ($X_{tx} < -X_O$), power circulates from the inductive branch to the capacitive branch; with very high inductive loads ($X_{tx} > X_O$), power circulates from the capacitive branch to the inductive branch.

The reactance steering network can be implemented in many different ways. In general, the system steers power towards the inductive branch or capacitive branch to seamlessly compensate the reactance variation. Both the two HF inverters see pure resistive load. Compared to conventional designs, the proposed RSN architecture has the following advantages:

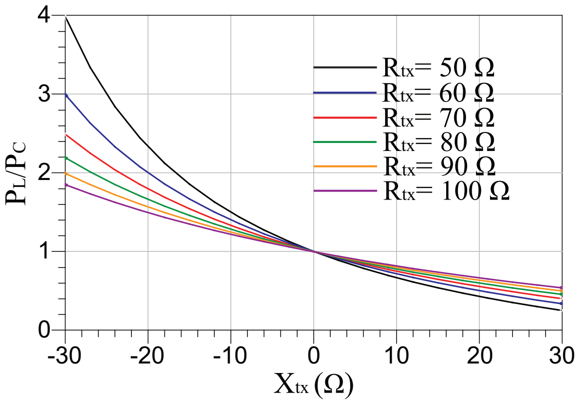


Fig. 8. Power ratio $P_L/P_C$ as a function of the load impedance $Z_{tx}$ for a specific $K_{LC}$ value and $\Delta_{LC}$ value. This power ratio can be used to estimate the load impedance to enable maximum power point tracking and maximum efficiency tracking.

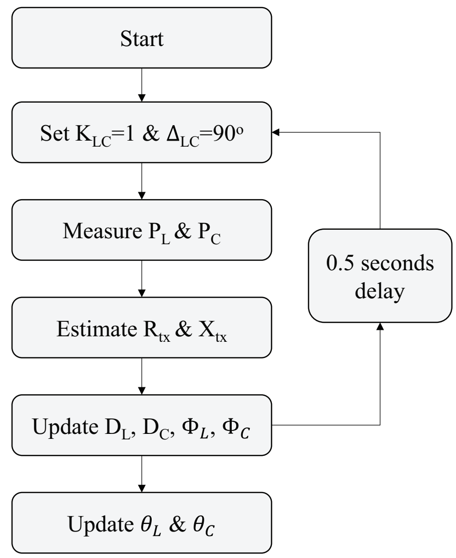


Fig. 9. Control flow chart of the impedance estimation. The impedance estimation process is repeated every 0.5 seconds.

- It can seamlessly compensate an arbitrary load impedance range and maintain pure resistive load;
- It requires very few additional component compared to a push-pull Class-E inverter;
- It has smooth transient behavior for load variation with no mode-switching spikes or harmonics;
- The dc-dc converters in the RSN are reused to drive a LF transmitter.

### B. Load Impedance Estimation and Control

Load impedance estimation allows WPT systems to operate at maximum power point and maintain high efficiency. Sophisticated ac voltage and/or current sensing circuitry are usually needed in existing high frequency designs. The unique configuration of the RSN architecture allows low cost load impedance estimation for WPT without ac voltage/current sensors. The load impedance can be estimated with simple circuitry by comparing the dc power delivered by the two inverter branches. Based on Eq. (1) and Eq. (2), the input dc power of the two inverter branches, $P_C$ and $P_L$, are

$$P_C = \frac{V_C^2(R_{tx} - K_{LC}(R_{tx}\cos(\Delta_{LC}) - X_{tx}\sin(\Delta_{LC})))}{2X_O^2}, \tag{7}$$

$$P_L = \frac{V_L^2(R_{tx} - \frac{1}{K_{LC}}(R_{tx}\cos(\Delta_{LC}) + X_{tx}\sin(\Delta_{LC})))}{2X_O^2}. \tag{8}$$

The ratio of the power delivered by the two branches is:

$$\frac{P_L}{P_C} = K_{LC}^2\frac{\eta_C(R_{tx} - \frac{1}{K_{LC}}(R_{tx}\cos(\Delta_{LC}) + X_{tx}\sin(\Delta_{LC})))}{\eta_L(R_{tx} - K_{LC}(R_{tx}\cos(\Delta_{LC}) - X_{tx}\sin(\Delta_{LC})))}. \tag{9}$$

Here $\eta_L$ and $\eta_C$ are the efficiencies of the two dc-dc converters. Eq. (9) indicates that the load impedance $R_{tx}$ and $X_{tx}$ are closely related to the input dc power ratio $\frac{P_L}{P_C}$ for a given $\eta_L$, $\eta_C$, $K_{LC}$, and $\Delta_{LC}$. $\frac{P_L}{P_C}$ can be measured from the dc-dc converters with simple circuit and low cost.

Fig. 8 plots the relationship between the input dc power ratio $P_L/P_C$ and load impedance $Z_{tx} = R_{tx} + jX_{tx}$ for $K_{LC} = 1$ and $\Delta_{LC} = 90°$. The load resistance can be estimated with the total input power $P_L + P_C$ and the voltage amplitudes. Assume the efficiencies of the two inverters are the same, the load input impedance $X_{tx}$ can be estimated with $P_L/P_C$ using Fig. 8. Fig. 9 shows the control flow chart for the load impedance estimation. The input power of the L and C branches are sampled and the power ratio are calculated. Through a look-up table, the desired duty cycles ($D_L$ and $D_C$) and the driving phases ($\phi_L$ and $\phi_C$) can be obtained to control the dc-dc converters and Class-E inverters based on the calculated power ratio $P_L$ and $P_C$.

### C. Low Frequency Full Bridge Transmitter

One way to implement the two dc-dc converters is to build them as two buck converters with two half-bridge inverters (Fig. 5). The two half-bridge inverters can drive a LF coil as a phase-shifted full bridge, while at the same time modulate the dc voltages $M_C$ and $M_L$ for the HF inverters. The LF power transfer is controlled by the phase of the two LF inverters $\theta_L$ and $\theta_C$. The output $M_L$ and $M_C$ are controlled by $D_L$ and $D_C$. Fig. 10 shows the schematic of the dual-band transmitter with the RSN-based high frequency transmitter shaded. Here $R_{LFtx}$ and $X_{LFtx}$ are the resistance and reactance of the low frequency coils. In this circuit, $Q_1$ and $Q_2$ operate as one phase-shifted half-bridge, and $Q_3$ and $Q_4$ operate as the other phase-shifted half-bridge. The duty ratios of the two half-bridges modulate $M_C$ and $M_L$, and the phase difference between the two half-bridges modulates the power output of the LF transmitter.

Benefiting from the low pass filters at the output of the dc-dc converters and the input inductors of the Class-E inverters, the power delivered by LF transmitter and the HF transmitter are well-decoupled from each other. $\theta_C$ and $\theta_L$ modulate the LF transmitter, but have no impact on $M_C$ and $M_L$, and thus have no impact on the power delivery of the HF transmitter. Similarly, $\Phi_C$ and $\Phi_L$ modulate the HF transmitter, but have

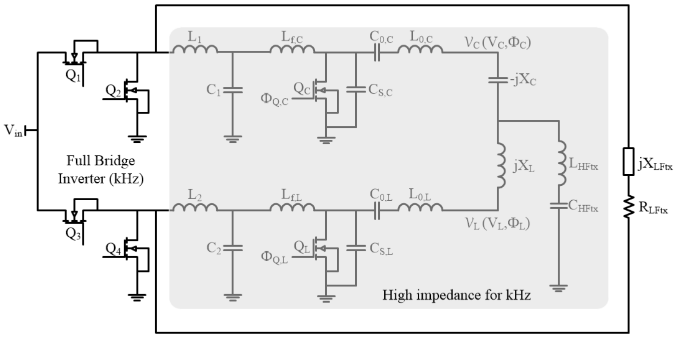


Fig. 10. Schematic of the dual-band transmitter with a phase-shifted full bridge LF transmitter, and a RSN-based HF transmitter. The two high frequency inverters look like two high impedance loads for the LF full bridge inverter.

TABLE I
PARAMETERS OF THE EXAMPLE DUAL-BAND RECTIFIER

| $L_{f1}$ | $C_{r1}$ | $L_{f2}$ | $C_{r2}$ | $C_{f1}$ | $C_{f2}$ |
|---|---|---|---|---|---|
| 1.2 $\mu$H | 500 pF | 1.2 $\mu$H | 500 pF | 20 $\mu$F | 20 $\mu$F |

no impact on the LF transmitter. When $D_C$ and $D_L$ are adjusted to modulate $M_C$ and $M_L$, $\theta_C$ and $\theta_L$ should be changed accordingly to maintain the power levels of the LF transmitter. Similar to [4], the two overlapped transmitter coils and the related resonant tanks are optimally tuned for 100 kHz and 13.56 MHz, respectively.

## IV. DUAL-BAND RECONFIGURABLE RECEIVER (DBRR)

In many application scenarios, a wireless power receiver may need to be compatible with multiple standards. The receivers also need to be compact and efficient with low component count. A full bridge synchronous rectifier can work at both high frequencies and low frequencies. However, the square-wave harmonic contents of the full bridge rectifier raise concerns for many portable applications. It is also difficult to drive the high-side switches in a full-bridge rectifier. One can use Class-E rectifiers at high frequencies to reduce the harmonic contents, but the inductance of the choke inductor is usually large.

Fig. 11a shows the topology of a dual-band reconfigurable receiver (DBRR). The rectifier in the receiver comprises two switches $Q_{r1}$ and $Q_{r2}$, two shunt capacitors $C_{r1}$ and $C_{r2}$, two RF choke inductors, two filter capacitors, and one switch $Q_s$ for mode selection. The dual-band rectifier can either work in the kHz range (e.g., 100 kHz), or work in the MHz range (e.g., 13.56 MHz), depending on if $Q_s$ is off or on. The parasitic capacitance of the diodes are absorbed into the shunt capacitors. Table I lists the component values of the proposed dual-band rectifier for 100 kHz and 13.56 MHz operation.

Fig. 11b and Fig. 11c illustrate the operation principles of the proposed rectifier in HF and LF, respectively. If $Q_s$ is kept ON, the rectifier functions as two Class-E half-wave rectifiers stacked in series. The rectifier receives power from the high frequency coil (i.e., 13.56 MHz). If $Q_s$ is kept OFF, the rectifier functions like a Class-D rectifier and receives power from the low frequency coil (i.e., 100 kHz). As shown in Fig. 11c, the RF choke inductors ($L_{f1}$ and $L_{f2}$) can be considered as short, and the shunt capacitors ($C_{r1}$ and $C_{r2}$) can be considered as open. $Q_s$ can be implemented as a low-speed switch in the controller IC. This inductor functions as a short circuit (with low impedance) at 100 kHz and a dc choke inductor (with high impedance) at 13.56 MHz.

Fig. 12a and Fig. 12b show the simulated voltage waveforms of $Q_{r1}$ and $Q_{r2}$ working at 13.56 MHz and 100 kHz, respectively. At high frequencies, the rectifier functions as two Class-E rectifiers stacked in series and the waveform of the voltage across the switches is half-wave sinusoidal. At low frequencies, the rectifier functions as one Class-D rectifier and the voltage across the switches is rectangular. In 100 kHz operation, the shunt capacitors may resonate with the RF choke inductors, resulting in a high frequency ripple at $V_{Q_{r1}}$ and $V_{Q_{r2}}$. One can reduce the oscillation by using a small $C_r$ at the cost of higher distortion at 13.56 MHz or using a small $L_f$ at the cost of higher ac current across the inductors. Fig. 12c and Fig. 12d show the simulated waveforms of the current and voltage of the mode selection switch at 13.56 MHz and 100 kHz, respectively. The blue lines are the dc output current and dc output voltage, respectively. The peak current flowing through $Q_s$ is twice of the dc output current. The voltage across the mode selection switch is same as that of the switch $Q_r$, which can be used to choose the current and voltage rating of the switch $Q_s$.

Fig. 12e and Fig. 12f show the simulated total harmonic distortion (THD) and the ratio of the switch peak voltage to the output voltage (the voltage stress of $Q_{r_1}$ and $Q_{r_2}$), and the input impedance of the dual-band rectifier with different $C_r$ values. The THD and the switch voltage stress can be reduced by increasing the $C_r$. However, a larger $C_r$ will reduce the input resistance of the rectifier, which may increase the conduction loss in the receiving coil, the RF choke inductor, and the rectifier switches.

The design principles of the dual-band rectifier are:

- The shunt capacitor $C_r$ should be designed on the THD requirement, voltage stress, and the ac self-resistance of the receiving coil;
- The mode selection switch $Q_s$ should be implemented as a low-speed switch with low on-resistance. Its voltage rating is the same as the two high speed switches $Q_{r_1}$ and $Q_{r_2}$;
- The inductors should be designed so that they function as RF choke inductors at high frequencies and function as shorts at low frequencies;
- The output filter capacitor $C_f$ should be big enough to eliminate the output voltage ripple.

At high frequencies (e.g., 13.56 MHz), the optimal duty ratio of the switches in the dual-band rectifier depends on the load impedance. Fig. 13a and Fig. 13b show the optimal duty ratio and voltage stress of the switches for a range of $R_L$. The optimal duty ratio decreases as $R_L$ increases. Since the dual-band rectifier functions as two series-stacked Class-E half-wave current-driven rectifier, the voltage stress of each high frequency switch is only one half of the voltage stress of a conventional Class-E current-driven rectifier [30]. For low

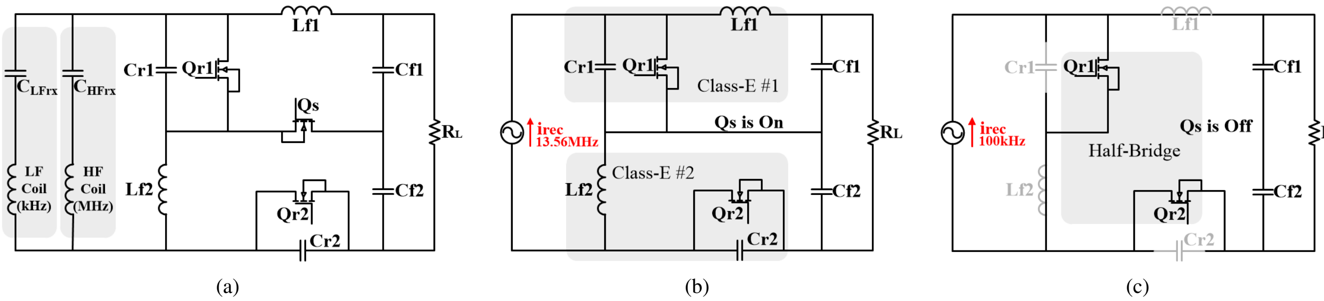


Fig. 11. Topology of the dual-band receiver: (a) Schematic of the dual-band receiver; (b) Schematic of the rectifier when it operates at high frequency with $Q_S$ ON; (c) Schematic of the rectifier when it operates at low frequency with $Q_S$ OFF.

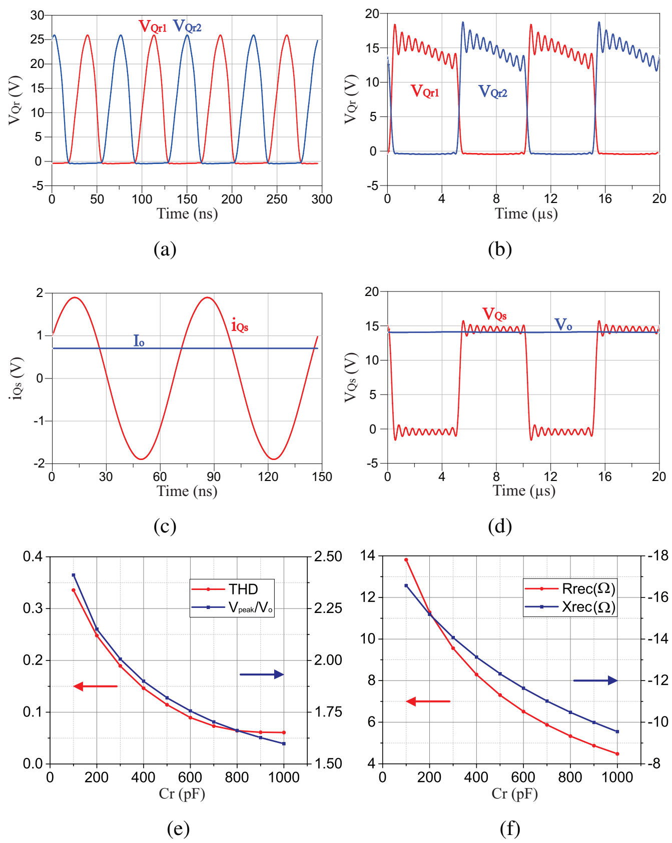


Fig. 12. (a) Simulated drain-to-source voltage of $Q_r$ at 13.56 MHz; (b) Simulated drain-to-source voltage of $Q_r$ at 100 kHz; (c) Simulated current waveform of the mode selection switch $Q_s$ at 13.56 MHz; (d) Simulated voltage waveform of the mode selection switch $Q_s$ at 100 kHz; (e) Simulation THD and the ratio of the switch peak voltage to the output voltage (voltage stress of the switch); and (f) Simulated rectifier input impedance.

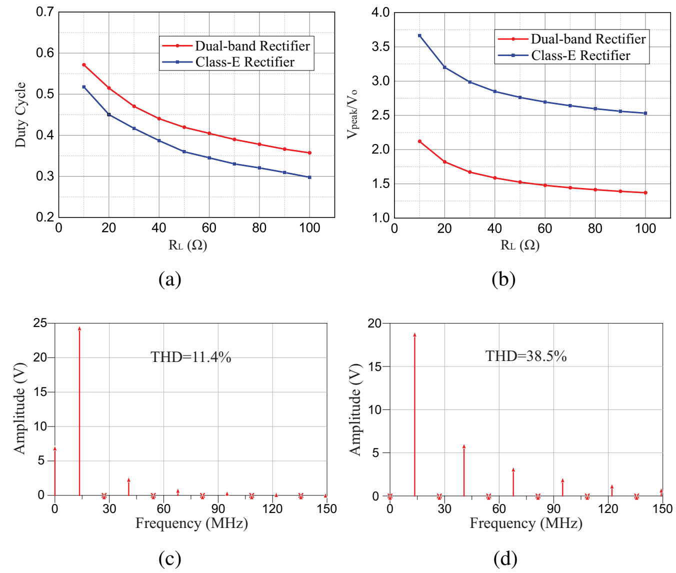


Fig. 13. (a) Simulated optimal rectifier duty cycle at 13.56 MHz; (b) Simulated switch voltage stress at 13.56 MHz; (c) Simulated THD of the dual-band rectifier at 13.56 MHz; (d) Simulated THD of the full bridge rectifier at 13.56 MHz.

frequency operation, the voltage stress of the two switches is identical to that of a half bridge rectifier. Fig. 13c and Fig. 13d show the simulated total harmonics distortion (THD) of the dual-band rectifier and the full bridge rectifier operating at 13.56 MHz. As expected, the dual-band reconfigurable rectifier works as two series-connected Class-E rectifiers and offers significantly lower THD than a full bridge rectifier.

Compared to a system with two separate rectifiers designed for one frequency each, the proposed dual-band rectifier offers the following advantages:

1) High efficiency at both kHz and MHz operation.
2) Lower voltage stress than a Class E rectifier, and lower harmonic distortion than a full bridge rectifier.
3) Very low component count (the dual-band rectifier only has one additional low speed switch $Q_s$ than a Class-E full-wave rectifier or a half-bridge rectifier).
4) Simple sensing, control and gate drive circuitry. The HF and LF sensing and control circuitry, as well as the mode-selection switch can be integrated in a single chip.

In summary, the proposed dual-band rectifier is a promising option for future practical designs where high performance and low component count are needed. The key principles of this rectifier is to merge high efficiency low frequency rectifiers (e.g., Class-D) with low distortion high frequency rectifiers (e.g., Class-E), without increasing the component count and the device stress. When designing this rectifier, the LF rectifier and HF rectifier should be jointly optimized so that they share the same loss budget when delivering the same amount of power with the same thermal limit.

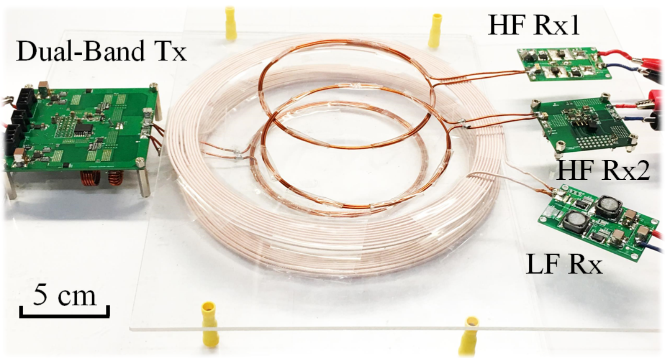


Fig. 14. The prototype dual-band WPT system with a RSN-based transmitter, a pair of HF coils, a pair of LF coils, and one active HF receiver, one passive HF receiver, and one passive LF receiver.

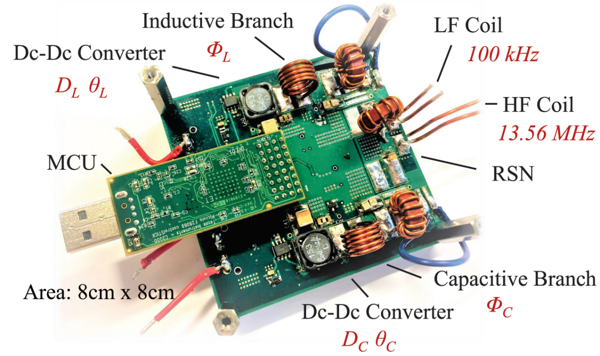


Fig. 16. The dual-band transmitter with two dc-dc converters, a push-pull Class-E inverter, a reactance steering network, and a microcontroller (TI F28069). Power is jointly delivered by the inductive branch and the capacitive branch.

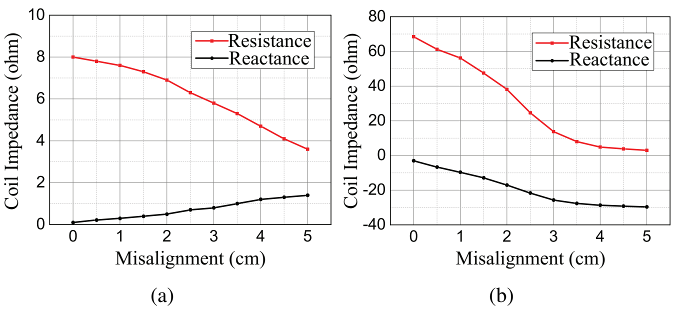


Fig. 15. Measured input impedances of the LF and HF coils against coil misalignment: (a) the input impedance of the LF coil; (b) the input impedance of the HF coil.

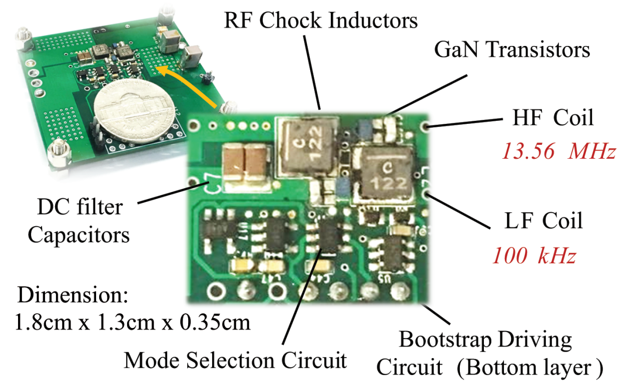


Fig. 17. The active dual-band rectifier with two GaN transistors, the mode selection and bootstrap driving circuits. The power density is 300 W/inch$^3$.

## V. Experimental Verification

Fig. 14 shows a prototype dual-band WPT system comprising a 100 kHz transmitter, a 13.56 MHz transmitter, a 100 kHz receiver, and two 13.56 MHz receivers (one passive and one active). The operating frequency, 13.56 MHz from the ISM band, is chosen to demonstrate the effectiveness of the proposed architecture with a more compact prototype, and to explore the limitations of the proposed architecture. Measured parameters of the coupling coils are listed in Table II. Fig. 15 shows the measured input impedances of the LF and HF coils under a varying misalignment. Here the impedance variation is jointly determined by the self- and mutual-inductance, cross coupling, compensation capacitance, and load impedance of the LF and HF coils. The impedance of the HF coil highly depends on the coil misalignment. Fig. 16 shows a picture of the dual-band transmitter. Key parameters of the dual-band transmitter are listed in Table III. $L_{f,C}$ and $L_{f,L}$ are designed to resonate with $C_{S,C}$ and $C_{S,L}$ following the method described in [17]. The resonant frequency of the output tank of the two Class-E inverters, $L_{0,C}$ and $C_{0,C}$, $L_{0,L}$ and $C_{0,L}$, are 13.56 MHz. The two HF switches are implemented as GaN transistors (GS66504B). The output capacitance of the two HF switches are absorbed into $C_{S,C}$ and $C_{S,L}$. Fig. 17 shows a picture of the dual-band reconfigurable rectifier.

A 100 kHz receiver and a 13.56 MHz receiver are designed and tested to evaluate the performance of the dual-band WPT system. The dual-band reconfigurable rectifier (Fig. 17) is used as the 100 kHz receiver when $Q_s$ is off and as the 13.56 MHz receiver when $Q_s$ is on, respectively. The diameters of the HF coil and the LF coil are 10 cm and 20 cm, respectively. The distance between the transmitting coil and the receiving coils is 2.8 cm. The maximum horizontal misalignment is 5 cm. Fig. 18 shows the ZVS operation of the HF switches with $Z_{tx}$ ($= 14 - j26\ \Omega$). The system delivers 10 W with and without RSN at 13.56 MHz. The RSN enables ZVS of both switches with appropriate phase and amplitude modulation. Fig. 19 shows the measured end-to-end efficiency of the 100 kHz WPT system and the 13.56 MHz WPT system with and without using the RSN. As shown in Fig. 19, the system with the RSN achieves higher efficiency than the system without the RSN across the entire misalignment range. Up to 13% of efficiency improvements are observed with significant load reactance (e.g., with 5 cm misalignment). We also observed that the presence of LF coil reduces the quality factor of the HF coil, thus reduces the system efficiency with large coil misalignments. The efficiency of the dual-band WPT system can be improved by increasing the Q of the dual-band coils (through better materials and better 2D layout).

Fig. 20 and Fig. 21 show the measured power and efficiency of the LF and HF systems working together. The system can independently modulate the power delivered by the LF coil and HF coil. The power delivered by the LF coil is controlled

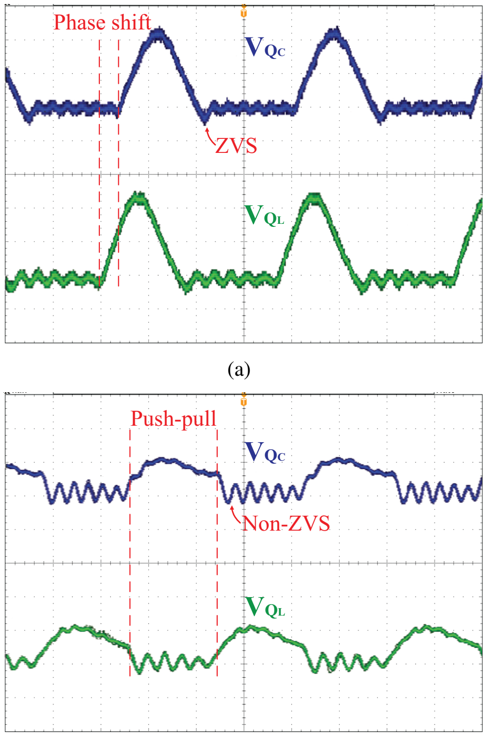


(b)

Fig. 18. Measured drain-to-source voltage waveforms of the two HF switches (30 V/div, 20 ns/div): (a) the switches achieve ZVS with RSN and phase shift, and (b) the switches lost ZVS without RSN and phase shift (operate as a traditional push-pull Class-E inverter).

TABLE II
PARAMETERS OF THE COUPLING COILS

| | | | | | |
|---|---|---|---|---|---|
| $L_{tx,LF}$ | $r_{tx,LF}$ | $C_{tx,LF}$ | $L_{rx,LF}$ | $r_{rx,LF}$ | $C_{rx,LF}$ |
| 36 $\mu$H | 0.2 $\Omega$ | 70 nF | 36 $\mu$H | 0.2 $\Omega$ | 80 nF |
| $L_{tx,HF}$ | $r_{tx,HF}$ | $C_{tx,HF}$ | $L_{rx,HF}$ | $r_{rx,HF}$ | $C_{rx,HF}$ |
| 3.5 $\mu$H | 2 $\Omega$ | 40 pF | 1.2 $\mu$H | 0.5 $\Omega$ | 130 pF |

TABLE III
PASSIVE COMPONENT VALUES OF THE DUAL-BAND TRANSMITTER.

| | | | | | | |
|---|---|---|---|---|---|---|
| $L_{f,C}$ | $L_{0,C}$ | $C_{S,C}$ | $C_{0,C}$ | $C_{RSN}$ | $C_1$ | $L_1$ |
| 200 nH | 1650 nH | 260 pF | 83 pF | 397 pF | 20 uF | 10 uH |
| $L_{f,L}$ | $L_{0,L}$ | $C_{S,L}$ | $C_{0,L}$ | $L_{RSN}$ | $C_2$ | $L_2$ |
| 200 nH | 1650 nH | 260 pF | 83 pF | 350 nH | 20 uF | 10 uH |

by the duty ratio $D_L$, $D_C$, and the phase shift $\theta_L$ and $\theta_C$. The power delivered by the HF coil is controlled by the intermediate voltage $M_L$, $M_C$, and the phase $\Phi_L$ and $\Phi_C$. The operation of the two frequency bands are independent from each other with negligible cross-coupling effects. As shown in Fig. 20, by keeping $D_L$, $D_C$, $\Phi_L$, $\Phi_C$ as constants, and modulating the phase difference between $\theta_L$ and $\theta_C$ from 0 to $2\pi$, the power transferred at 100 kHz (Po_LF) can be modulated between 0 W to 20 W, and the power transferred at 13.56 MHz (Po_HF) can be kept constant at 10 W. Similarly, as shown in Fig. 21, one can keep the power transferred at 100 kHz constant at 10 W, and modulates the power transferred at 13.56 MHz from 0 W to 15 W by changing the

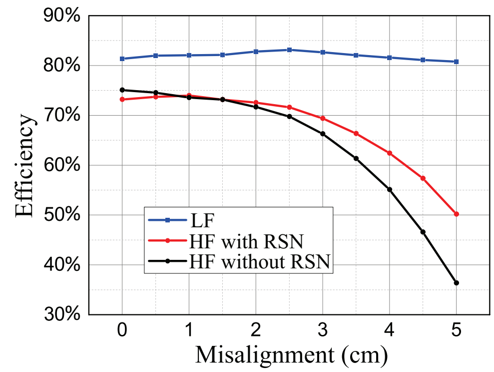


Fig. 19. Measured end-to-end efficiency of the dual-band WPT system. The radius of the HF coil is 5 cm, and the radius of the LF coil is 10 cm. The RSN significantly improved the system efficiency when the coil misalignment is large.

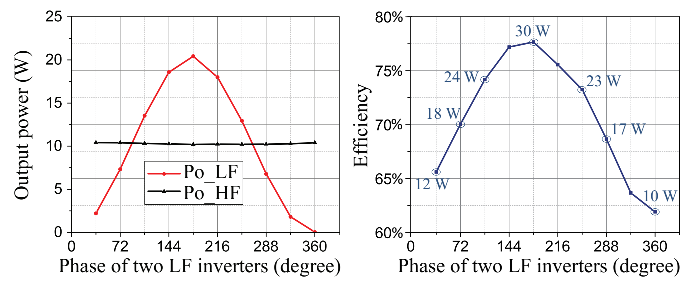


(a) (b)

Fig. 20. Measured power and overall efficiency of the dual-band WPT system (HF and LF systems together). The system can maintain the power delivered at the high frequency (Po_HF) and modulate the power delivered at the low frequency (Po_LF). This is achieved by modulating the phase shift of the two LF inverters ($\theta_L$ and $\theta_C$).

duty ratio of the LF inverters. The measured efficiencies of the HF and LF transmitters working together are also shown in Fig. 20 and Fig. 21. When delivering 10 W of power at 13.56 MHz, and delivering 20 W of power at 100 kHz, the system reaches a maximum end-to-end efficiency of 77.7%.

Fig. 22 shows the measured drain-to-source voltage waveforms of the Class-E inverters with and without the RSN. The coil misalignment changes from 1 cm to 5 cm. The Class-E inverters operate in ZVS across the entire coil misalignment range with the RSN. $D_L/D_C$ and $\Delta_{LC}$, are automatically selected from a look-up table according to the measured dc power ratio $P_L/P_C$ (following Fig. 9).

The rectifiers reported in the previous measurement results were implemented with passive diodes. To further improve the system end-to-end efficiency, a dual-band rectifier implemented with synchronous GaN transistors is built and tested (Fig. 11). The dimension of the active rectifier is 1.8 cm $\times$ 1.3 cm. The driving and auxiliary circuitry are all included. Based on the analysis in Section IV, the shunt capacitors of the dual-band rectifier $C_{r1}$ and $C_{r2}$ are 500 pF and the ratio $V_{peak}/V_o$ is about 1.82 (Fig. 12). The maximum dc output voltage of $Q_{r1}$ and $Q_{r2}$ ($V_{DS}$=40 V) is about 22 V and the maximum output power is 15 W at 13.56 MHz. A low cost and low on-resistance MOSFET ECH8420 is used as the mode selection switch $Q_s$. The RF choke inductors $L_{r1}$ and

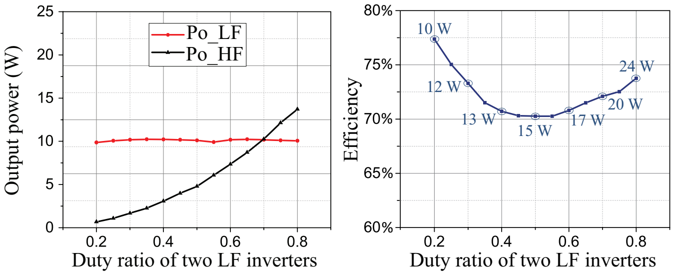


(a) (b)

Fig. 21. Measured power and overall efficiency of the dual-band WPT system (HF and LF systems together). The system can maintain the power delivered at the low frequency (Po_LF) and modulate the power delivered at the high frequency (Po_HF). This is achieved by modulating the duty ratios of the two LF inverters ($D_L$ and $D_C$).

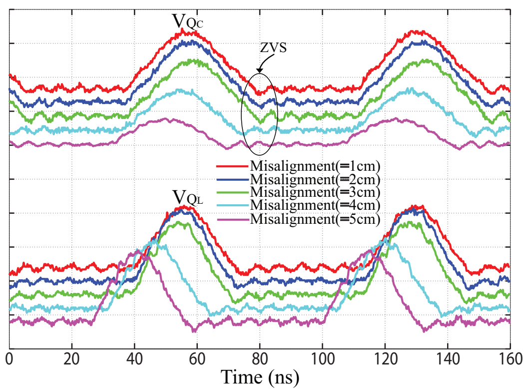


(a)

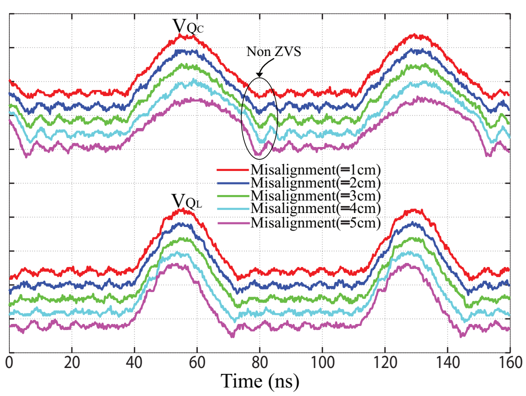


(b)

Fig. 22. Measured drain-to-source voltage waveforms of the Class-E inverters with the coil misalignment changing from 1 cm to 5 cm: (a) with phase shift and ZVS (50V/div); (b) without phase shift and non-ZVS (50V/div).

$L_{r2}$ are chosen as 1.2 $\mu$H which behave as high impedance (about 102j $\Omega$) at 13.56 MHz to block the high frequency current (reduce the ac power loss). They behave as short at 100 kHz. Fig. 23 shows the measured waveforms of the dual-band rectifier when working at HF and LF, respectively. The measured waveforms closely match with simulations (Fig. 12). Fig. 24 shows the thermal images of the active dual-band rectifier when receiving 15 W.

Fig. 25a compares the measured dc-dc efficiency of the WPT system at 13.56 MHz with and without synchronous

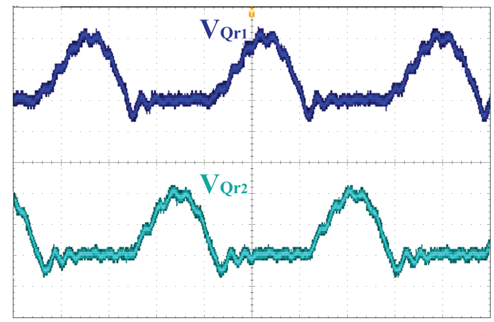


(a)

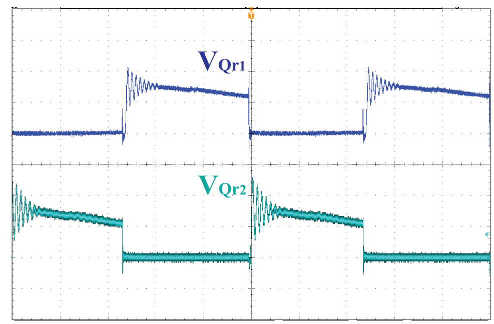


(b)

Fig. 23. Measured waveforms of the active dual-band rectifier: (a) drain-to-source voltage at 13.56 MHz (10V/div, 20ns/div); (b) drain-to-source voltage at 100 kHz (10V/div, 2$\mu$s/div).

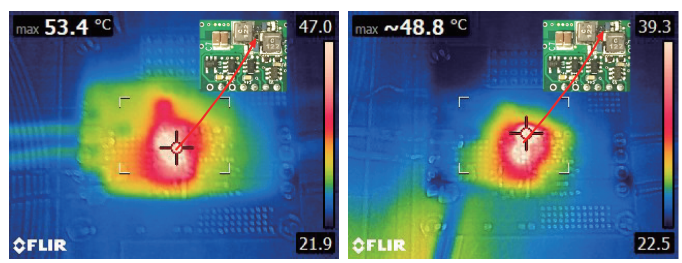


(a) (b)

Fig. 24. Thermal images of the active dual-band rectifier with the output power of 15 W: (a) 13.56 MHz operation; (b) 100 kHz operation.

rectification. Fig. 25b does the same comparison for 100 kHz operation. As expected, synchronous rectification significantly improves the system efficiency across the full power range. Table IV lists a comprehensive comparison among this work and existing works. This work has four key contributions: a) the reactance steering network which can maintain the ZVS operation for the HF inverters across a wide load impedance range; b) a GaN-based dual-band reconfigurable rectifier; c) a load impedance estimation and control method; and d) a full demonstration of the dual band WPT architecture and topology with shared switches and lower component count than conventional solutions.

## VI. Conclusions

A dual-band multi-receiver WPT architecture targeting large coil misalignment and significant impedance variation is p-resented in this paper. This architecture is developed based

TABLE IV
COMPARISON AGAINST OTHER DUAL-BAND WPT DESIGNS

| | Frequency | Power (W) | Efficiency | Misalignment | Control | Other Technologies |
|---|---|---|---|---|---|---|
| [7] | 6.78 MHz/100-200 kHz | 5/5 | 66%/72% | n/a | n/a | n/a |
| [8] | 6.78 MHz/100-315 kHz | 5/5 | 65%/65% | n/a | n/a | n/a |
| [9] | 13.56 MHz/110 kHz | n/a | n/a | 10 mm | n/a | n/a |
| [10] | 6.78 MHz/200 kHz | 9/7.4 | 78%/70.6% | n/a | n/a | n/a |
| [11] | 6.78 MHz/87-300 kHz | 10/10 | 65%/65% | n/a | MFPWM | n/a |
| [12] | 6.78 MHz/200 kHz | n/a | 74%/55% (coil) | 20 mm | n/a | n/a |
| [29] | 13.56 MHz/100 kHz | 10/10 | 72.5%/81% | 30 mm | n/a | RSN |
| This work | 13.56 MHz/100 kHz | 15/15 | 74.8%/82.5% | 50 mm | Look-up Table | RSN and DBRR |

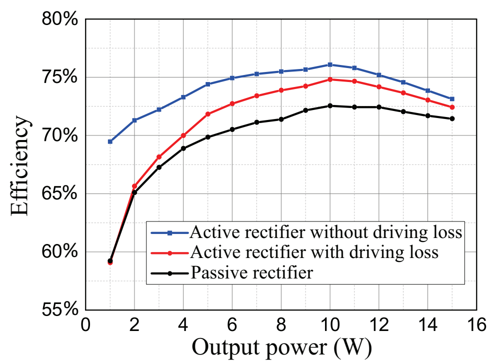


(a)

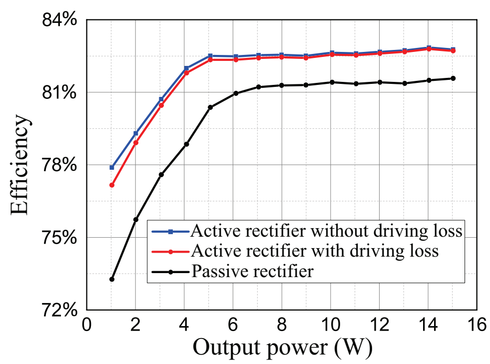


(b)

Fig. 25. Measured efficiency of the dual-band reconfigurable rectifiers: (a) 13.56 MHz operation; (b) 100 kHz operation.

on a novel reactance steering network (RSN) that can precisely compensate an arbitrary load reactance by dynamically steering the power between two inverter branches. We developed the theory of RSN and presented a design method that can cover a wide reactance variation range. To justify the additional component needed by the RSN, this paper also presents the topology and operation principles of a dual-band reconfigurable rectifier that can achieve high performance at both 100 kHz and 13.56 MHz. The dual-band inverter and dual-band receiver function together as a complete dual-band WPT system with high performance. The effectiveness of the proposed architecture is verified by a 30 W dual-band WPT prototype that can efficiently and independently power multiple 100 kHz and 13.56 MHz receivers with significant coil misalignment and load variation. The RSN architecture and the dual-band reconfigurable receiver are applicable to a wide range of WPT enabled applications.

## ACKNOWLEDGMENT

This work was supported in part by the National Science Foundation under award number #1847365, in part by the the Andlinger Center for Energy and the Environment, Princeton University, and in part by the Siebel Energy Institute.

## REFERENCES

[1] S. Y. R. Hui, W. Zhong and C. K. Lee, "A Critical Review of Recent Progress in Mid-Range Wireless Power Transfer," *IEEE Transactions on Power Electronics*, vol. 29, no. 9, pp. 4500-4511, Sept. 2014.

[2] A. P. Hu, *Wireless/Contactless Power Supply: Inductively coupled resonant converter solutions*, Saarbrucken, Germany: VDM Publishing, 2009.

[3] G. Buja, M. Bertoluzzo and K. N. Mude, "Design and Experimentation of WPT Charger for Electric City Car," *IEEE Transactions on Industrial Electronics*, vol. 62, no. 12, pp. 7436-7447, Dec. 2015.

[4] B. H. Choi, V. X. Thai, E. S. Lee, J. H. Kim and C. T. Rim, "Dipole-Coil-Based Wide-Range Inductive Power Transfer Systems for Wireless Sensors," *IEEE Transactions on Industrial Electronics*, vol. 63, no. 5, pp. 3158-3167, May 2016.

[5] T. Campi, S. Cruciani, F. Palandrani, V. De Santis, A. Hirata and M. Feliziani, "Wireless Power Transfer Charging System for AIMDs and Pacemakers," *IEEE Transactions on Microwave Theory and Techniques*, vol. 64, no. 2, pp. 633-642, Feb. 2016.

[6] S. Li, W. Li, J. Deng, T. D. Nguyen, and C. C. Mi, "A double-sided LCC compensation network and its tuning method for wireless power transfer," *IEEE Transactions on Vehicular Technology*, vol. 64, no. 6, pp. 2261-C2273, June 2015.

[7] P. S. Riehl et al., "Wireless Power Systems for Mobile Devices Supporting Inductive and Resonant Operating Modes," *IEEE Transactions on Microwave Theory and Techniques*, vol. 63, no. 3, pp. 780-790, March 2015.

[8] M. d. Rooij and Y. Zhang, "A 10 W Multi-Mode Capable Wireless Power Amplifier for Mobile Devices," *PCIM Asia 2016; International Exhibition and Conference for Power Electronics, Intelligent Motion, Renewable Energy and Energy Management*, Shanghai, China, 2016, pp. 1-8.

[9] T. Sekiguchi, H. Odanaka, Y. Okano and S. Ogino, "Study on the effective loading method of the magnetic sheet for NFC/WPT dual-band antenna," *2016 International Symposium on Antennas and Propagation (ISAP)*, Okinawa, 2016, pp. 946-947.

[10] D. Ahn and P. P. Mercier, "Wireless Power Transfer With Concurrent 200-kHz and 6.78-MHz Operation in a Single-Transmitter Device," *IEEE Transactions on Power Electronics*, vol. 31, no. 7, pp. 5018-5029, July 2016.

[11] C. Zhao and D. Costinett, "GaN-Based Dual-Mode Wireless Power Transfer Using Multifrequency Programmed Pulse Width Modulation," *IEEE Transactions on Power Electronics*, vol. 64, no. 11, pp. 9165-9176, Nov. 2017.

[12] M. Kung and K. Lin, "Dual-Band Coil Module With Repeaters for Diverse Wireless Power Transfer Applications," *IEEE Transactions on Microwave Theory and Techniques*, vol. 66, no. 1, pp. 332-345, Jan. 2018.

[13] N. O. Sokal and A. D. Sokal, "Class E-A new class of high-efficiency tuned single-ended switching power amplifiers," *IEEE Journal of Solid-State Circuits*, vol. 10, no. 3, pp. 168-176, Jun 1975.

[14] Y. Han, O. Leitermann, D.A. Jackson, J.M. Rivas, and D.J. Perreault, "Resistance compression networks for radio-frequency power conversion," *IEEE Transactions on Power Electronics*, Vol. 22, No.1, pp. 41-53, Jan. 2007.

[15] J. Choi, J. Xu, R. Makhoul and J. M. Rivas Davila, "Implementing an impedance compression network to compensate for misalignments in a wireless power transfer system," *IEEE Transactions on Power Electronics*, early access.

[16] D. J. Perreault, "A new power combining and outphasing modulation system for high-efficiency power amplification," *IEEE Transactions on Circuits and Systems I: Regular Papers*, vol. 58, no. 8, pp. 1713-1726, Aug 2011.

[17] L. Roslaniec, A. S. Jurkov, A. A. Bastami, and D. J. Perreault, "Design of single-switch inverters for variable resistance/load modulation operation," *IEEE Transactions on Power Electronics*, vol. 30, no. 6, pp. 3200-3214, June 2015.

[18] Jie Lu, David J. Perreault, David M. Otten, and Khurram Afridi. "Impedance Control Network Resonant DC-DC Converter for Wide-Range High-Efficiency Operation," *IEEE Transactions on Power Electronics*, Vol. 31, No.7, July 2016.

[19] S. J. Gunter, K. K. Afridi, D. M. Otten, R. A. Abramson and D. J. Perreault, "Impedance control network resonant step-down DC-DC converter architecture," *IEEE Energy Conversion Congress and Exposition (ECCE)*, Montreal, QC, 2015, pp. 539-547.

[20] W. Inam, K. K. Afridi and D. J. Perreault, "High Efficiency Resonant DC/DC Converter Utilizing a Resistance Compression Network," *IEEE Transactions on Power Electronics*, vol. 29, no. 8, pp. 4126-4135, Aug. 2014.

[21] Ashish Kumar, Sreyam Sinha, Alihossein Sepahvand, and Khurram Afridi. "Improved Design Optimization for High-Efficiency Matching Networks," *IEEE Transactions on Power Electronics*, Vol. 33, No. 1, January 2018.

[22] S. Liu, M. Liu, S. Han, X. Zhu, and C. Ma, "Tunable Class $E^2$ dc-dc converter with high efficiency and stable output power for 6.78 MHz wireless power transfer," *IEEE Transactions on Power Electronics*, vol. 33, no. 8, pp. 6877-6886, Aug. 2018.

[23] S. Sinha, A. Kumar and K. K. Afridi, "Active variable reactance rectifier: A new approach to compensating for coupling variations in wireless power transfer systems," *IEEE Workshop on Control and Modeling for Power Electronics (COMPEL)*, Stanford, CA, 2017, pp. 1-8.

[24] S. Cochran, F. Quaiyum, A. Fathy, D. Costinett and S. Yang, "A GaN-based synchronous rectifier for WPT receivers with reduced THD," *IEEE PELS Workshop on Emerging Technologies: Wireless Power Transfer (WoW)*, Knoxville, TN, 2016, pp. 81-87.

[25] M. Chen, "Merged multi-stage power conversion: A hybrid switched capacitor/magnetics approach," Ph.D. dissertation, Electr. Eng. Comput. Sci. Dept., Massachusetts Inst. Technol., Cambridge, MA, USA, 2015.

[26] M. Chen, K. K. Afridi, S. Chakraborty, and D. J. Perreault, "Multitrack Power Conversion Architecture," *IEEE Transactions on Power Electronics*, vol. 32, no. 1, pp. 325-340, Jan. 2017.

[27] M. Chen, S. Chakraborty, and D. J. Perreault, "Multitrack Power Factor Correction Architecture," *IEEE Transactions on Power Electronics*, early access.

[28] H. Kim, H. Chen, D. Maksimovic, and R. Erickson, "Design of a high efficiency 30 kW boost composite Converter," *Proc. IEEE Energy Convers. Cong. Expo. (ECCE)*, Sep. 2024, 2015, pp. 42434250.

[29] M. Liu and M. Chen, "Dual-Band Multi-Receiver Wireless Power Transfer with Reactance Steering Network," *IEEE PELS Workshop on Emerging Technologies: Wireless Power Transfer (Wow)*, Montreal, QC, 2018, pp. 1-6.

[30] J. A. S-Gonzlez, K. M. Elbaggari, K. K. Afridi and D. J. Perreault, "Design of Class E Resonant Rectifiers and Diode Evaluation for VHF Power Conversion," *IEEE Transactions on Power Electronics*, vol. 30, no. 9, pp. 4960-4972, Sept. 2015.

**Ming Liu** (S'15−M'17) received the B.S. degree from Sichuan University, Sichuan, China, in 2007, and the Ph.D. degree in electrical and computer engineering from the University of Michigan-Shanghai Jiao Tong University Joint Institute, Shanghai Jiao Tong University, Shanghai, China, in 2017.

He is currently a postdoctoral research fellow at Department of Electrical Engineering of Princeton University, Princeton, NJ, USA. His research interests include circuit topology and architecture, control strategy, optimization-based design methods for MHz wireless power transfer (WPT), and high frequency power electronics.

Liu was the recipient of the Top-10 Academic Star Award and Excellent PhD Thesis Award Nomination at Shanghai Jiao Tong University, and the Research Excellence Award from AirFuel Alliance.

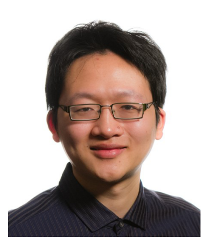

**Minjie Chen** (S'10−M'15) received the B.S. degree from Tsinghua University, Beijing, China, in 2009, and the S.M., E.E., and Ph.D. degrees from Massachusetts Institute of Technology (MIT), Cambridge, MA, USA, in 2012, 2014, and 2015.

He was a Postdoctoral Research Associate at MIT in 2016. He joined the Department of Electrical Engineering and Andlinger Center for Energy and the Environment at Princeton University as an Assistant Professor in 2017, where he leads the Princeton Power Electronics Research Lab (PowerLab). His research interests include high frequency power electronics, advanced power electronics architectures, power magnetics, and the design of high performance power electronics for emerging and important applications.

Chen was the recipient of the NSF CAREER Award, the outstanding Ph.D. thesis award from the Chorafas Foundation and MIT, two Transactions Prize Paper Awards from IEEE Transactions on Power Electronics, the Siebel Energy Institute Seed Grant, an IEEE ECCE best demonstration award, and a First Place Award from the Innovation Forum of Princeton University. He is an associate editor of the *IEEE Transactions on Power Electronics*, a guest associate editor of the *IEEE Journal of Emerging and Selected Topics in Power Electronics*, and an associate Technical Program Committee chair for *IEEE Energy Conversion Congress and Exposition*.